ALMA Observations of the Extraordinary Carina Pillars: HH 901/902

Geovanni Cortes-Rangel[1], Luis A. Zapata[1] , Jesús A. Toalá[1] , Paul T. P. Ho[2], Satoko Takahashi[3] , Adal Mesa-Delgado[4] , and Josep M. Masqué[5]

[1] Instituto de Radioastronomía y Astrofísica, Universidad Nacional Autónoma de México, P.O. Box 3–72, 58090, Morelia, Michoacán, México
l.zapata@irya.unam.mx
[2] Academia Sinica Institute of Astronomy and Astrophysics, P.O. Box 23-141, Taipei, 10617, Taiwan. East Asian Observatory, 666 N. A'ohoku Place, Hilo, Hawaii 96720, USA
[3] Joint ALMA Observatory, Alonso de Cordova 3108, Vitacura, Santiago, Chile. NAOJ Chile Observatory, Alonso de Cordova 3108, Vitacura, Santiago, Chile. Department of Astronomical Science, School of Physical Sciences, SOKENDAI (The Graduate University for Advanced Studies), Mitaka, Tokyo 181-8588, Japan
[4] Instituto de Astrofísica, Facultad de Física, Pontificia Universidad Católica de Chile, Av. Vicuña Mackenna 4860, 782-0436 Macul, Santiago, Chile
[5] Departamento de Astronomía, Universidad de Guanajuato, Apdo. Postal 144, 36000 Guanajuato, MÉxico

Abstract

We present Atacama Large Millimeter/Submillimeter Array 1.3 mm continuum and $C^{18}O(2-1)$, $N_2D^+(3-2)$, $^{13}CS(5-4)$, and $^{12}CO(2-1)$ line sensitive and high angular resolution ($\sim 0\rlap{.}''3$) observations of the famous Carina pillars and protostellar objects HH 901/902. Our observations reveal for the first time, the bipolar CO outflows and the dusty disks (plus envelopes) that are energizing the extended and irradiated Herbig–Haro (HH) objects far from the pillars. We find that the masses of the disks+envelopes are about 0.1 $M_\odot$ and that the bipolar outflows are between 10^{-3} and 10^{-4} $M_\odot$, which suggests that they could be low- or maybe intermediate-mass protostars. Moreover, we suggest that these young low-mass stars are likely embedded Class 0/I protostars with high-accretion rates. We also show the kinematics of the gas in the pillars together with their respective gas masses (0.1–0.2 $M_\odot$). We estimate that the pillars will be photoevaporated in 10^4 to 10^5 yr by the massive and luminous stars located in the Trumpler 14 cluster. Finally, given the short photoevaporated timescales and that the protostars in these pillars are still very embedded, we suggest that the disks inside of the pillars will be quickly affected by the radiation of the massive stars, forming proplyds, like those observed in Orion.

Unified Astronomy Thesaurus concepts: Proplyds (1296); Interstellar molecules (849); Aperture synthesis (53); Stellar jets (1607)

1. Introduction

The Carina Nebula is one most active star-forming regions in our Galaxy. This region contains nearly 100 O-type stars and tens of thousands of lower-mass young stars (Walborn 1973, 1995; Massey & Johnson 1993; Smith 2006; Feigelson et al. 2011; Povich et al. 2011; Preibisch et al. 2011), with the Trumpler (Tr) 14 and 16 massive clusters being one the most luminous regions within Carina. The clusters Tr 14 and 16 have ultraviolet (UV) luminosities about 20 and 60 times higher than $\theta 1$ Ori C located in the Orion Nebula (Smith & Brooks 2008). Hence, the Carina Nebula is an ideal laboratory to study the timescale of the photoevaporation of disks, envelopes, and molecular pillars located especially in the core of the massive clusters.

As a clear caphotoevapo/photoevaporating objects, using Atacama Pathfinder EXperiment (APEX) FLASH+ and CHAMP+ line observations, Sahai et al. (2012) reported an irradiated object with a cometary shape (CN 105−600) in the Carina star-forming region. They found that this externally irradiated object is not a classical proplyd as those reported in the Orion Nebula (O'Dell et al. 1993, 2008; Henney and O'Dell 1999), this object is instead a large and massive molecular globule (0.1–0.3 $M_\odot$) in which very compact disks and outflows are embedded. The young star inside of this globule has a mass of about 0.5 $M_\odot$ and total luminosity of about 10 $L_\odot$ (Sahai et al. 2012), corresponding to a low-mass young star. Haikala et al. (2017) also reported APEX observations of several globulettes in Carina; these globulettes are compact and denser than objects of similar mass in the Rosette Nebula.

There are however many more well-studied irradiate globules in the Carina Nebula, they include to HH 666, HH 1066, HH 900, and HH 1010 (Reiter & Smith 2013), which include interferometric millimeter observations. Given that different young massive star-forming regions have a very varied morphology, ages, and number of massive stars, these regions hold distinct kinds of irradiated interfaces (or globulettes) and their study is important as it will allow us to better understand the evolution of the young stars. A clear example is found in the Carina region (Hartigan et al. 2012), which contains a rich array of walls, pillars, and globules, and in the older Cyg OB2 association where mostly isolated globules are found.

Very recently, Mesa-Delgado et al. (2016) using Atacama Large Millimeter/Submillimeter Array (ALMA) Band 6 Long Baseline continuum observations reported the first direct imaging of protoplanetary disks in the star-forming region of Carina and studied their possible external strong photoevaporation. They detected a few protoplanetary disks (CN104-593 and CN105-600) in the highly obscured globules within the Carina Nebula and found no signs of disks near to the massive clusters Tr 14 and Tr 16. The disks have an average size of 120 au and total masses of 30 and 50 $M_{\rm Jup}$. The nondetection of millimeter emission above the 4σ threshold ($\sim 7 M_{\rm Jup}$) in the core of the massive cluster Tr 14 suggests evidence for rapid photoevaporative disk destruction in the cluster's harsh radiation field.

Bipolar molecular outflows and collimated optical jets are one of the phenomena associated with star formation (Bally 2016). The outflows are composed of swept-up molecular shells energized by neutral and atomic jets

containing molecules. As these molecular outflows escape from their parent molecular clouds to scales of some parsecs, they become mostly atomic or ionized and traced by Herbig–Haro (HH) objects revealed at optical wavelengths.

The HH 901/902 were first reported by Smith et al. (2010) using *Hubble Space Telescope* (*HST*)/Advanced Camera for Surveys (ACS) Hα observations. They cataloged the HH objects as irradiated bipolar jets. These objects are extremely bright and clear in their *HST* images (see their Figure 5). The dusty pillars from which HH 901 and 902 emerge are between Tr 14 and 16 clusters. Both HH objects axis are clearly perpendicular to the dusty pillars and are located at a distance of about 1.5′. to the south of the Tr 14 and about 7′. from Tr 16. These flows consist of a highly collimated (with opening angles of only a few degrees) chain of Hα-emitting knots with an extent of 16″ (0.18 pc) for HH 901 and an extent of 38″ (0.42 pc) for HH 902. Both flows are strongly irradiated by the massive clusters Tr 14 and 16. HH 901 and HH 902 both lie close to the plane of the sky with tilt angles of about 20° (Reiter & Smith 2014). Reiter & Smith (2013, 2014) suggested that these two jets are energized by intermediate-mass stars (2–8 $M_\odot$). However, these studies could not corroborate this interpretation due to the fact that the authors reported that the driving sources were not detected in the infrared (IR), probably because they were too embedded and because of inadequate angular resolution. Given these problems, the fits to the IR spectral energy distributions become very poor and the estimated luminosity is uncertain.

The HH 901/HH 902 objects have also been detected in H_2 (2.2 μm) and Brγ spectral lines by Hartigan et al. (2015). These observations represented the first detection of the molecular material associated with the HH objects. In particular, the H_2 emission is tracing the innermost parts of the outflow as can be seen in Figures 19 and 20 of Hartigan et al. (2015). Molecular material far from the exciting objects is probably destroyed by the UV radiation.

In this study, we have carried out new ALMA observations of the HH 901/HH 902 objects in order to better characterize their optical jets, disks, and molecular pillars. We reveal their compact molecular outflows, dusty disk, and envelopes, together with the kinematics of the pillars. We describe these results in more detail in the next sections.

2. Observations

The observations of the HH 901/902 protostellar objects were carried out with ALMA at Band 6 in 2018 January 1 and 4 (C43-6), and April 20 (C43-3) as part of the Cycle 5 program 2017.1.00912.S. The observations used 43 antennas with a diameter of 12 m, yielding baselines with projected lengths from 15 to 2516 m (11.5–1935 kλ) for C43-6 and 15–500 m (11.5–384.6 kλ) for C43-3. The primary beam at this frequency has an FWHM of about 25″, so that each object was covered with a single pointing at the sky position α(J2000) = 10^h 44^m 1^{s}7; δ(J2000) = −59° 30′32″0 for HH 902, and α(J2000) = 10^h 44^m 3^{s}5; δ(J2000) = −59° 31 2″0 for HH 901. The integration time on source (HH 901 and 902) for the C43-6 configuration was about 9 minutes and for the C43-3 configuration is about 3.5 minutes.

The continuum images were obtained by averaging line-free spectral channels of four spectral windows centered at 218.014 GHz(spw0), 219.578 GHz(spw1), 231.239 GHz (spw2), and 230.556 GHz(spw3). The total bandwidth for the continuum is about 4.3 GHz. These four spectral windows were centered to observe different molecular lines as the $C^{18}O(2-1)$ (ν_{rest} = 219.56035 GHz), $^{13}CS(5-4)$ (ν_{rest} = 231.22068 GHz), $N_2D^+(3-2)$ (ν_{rest} = 231.32186 GHz), and $^{12}CO(2-1)$ (ν_{rest} = 230.53800 GHz). We detected emission only from the lines $C^{18}O$, N_2D^+, and ^{12}CO with a channel spacing of 0.63 km s^{-1}. The thermal emission from these species can be seen in Figures 1–6.

The weather conditions were very good for these observations and stable with an average precipitable water vapor between 1.3 and 2.2 mm and an average system temperature around 90 K. The ALMA calibration included simultaneous observations of the 183 GHz water line with water vapor radiometers, used to reduce atmospheric phase fluctuations. Quasars J0904-5735 and J1107-4449 were used for the bandpass and flux calibrations. J1032-5917 was used for correcting the gain fluctuations.

The data were calibrated, imaged, and analyzed using the Common Astronomy Software Applications (CASA) Version 5.1. Imaging of the calibrated visibilities was done using the CLEAN and TCLEAN tasks. We concatenated the data from both dates for the C43-6 and C43-3 configurations with the CONCAT task. We used the ROBUST parameter of CLEAN in CASA set to uniform. The resulting image rms noise for the continuum was 50 μJy beam^{-1} at a angular resolution of 0″32 × 0″27 with a PA of −65° for both images. The ALMA theoretical rms noise for this configuration, integration time, and frequency is about 43 μJy beam^{-1}, which is very close to the value we obtain in the continuum images. For the line image rms noise we obtained a value of 6.5 mJy beam^{-1} km s^{-1} at a angular resolution of 0″31 × 0″26 with a PA of −64°. The ROBUST parameter was set also to uniform. The ALMA theoretical rms noise for this configuration, integration time, and frequency is about 4.3 mJy beam^{-1}, which is very close to the value we obtain in the line images. Phase self-calibration was attempted on the continuum images but the resulting maps did not improve significantly, so at this point we did not used the self-calibrated maps. We did not include the channel maps because they do not add extra information from that obtained from the moments maps.

3. Results and Discussion

3.1. HH 901

In Figure 1 we present the *HST*/ACS image from Smith et al. (2010) of the optical jet HH 901 overlaid with the ALMA high-velocity CO(2−1) and the 1.3 mm continuum emission. The CO emission reveals a bipolar and collimated outflow that is tracing the most inner part of the optical jet in an east–west orientation (with an approximate size of 5000 au). This map shows that the blueshifted emission is located toward an eastern orientation, while redshifted emission is to its western side. We integrate in radial velocities from +6.4 to −1.2 km s^{-1} for the redshifted emission, and from −8.2 to −14.6 km s^{-1} for the blueshifted emission for the CO outflow in the HH 901 object. The CO emission between −1.2 km s^{-1} and −8.2 km s^{-1} is associated with the dusty pillar as is shown in Figure 2. The LSR systemic velocity of the entire pillar associated with the object HH 901 is about −5.0 km s^{-1} (Figure 3). The radial velocities of the innermost CO outflow are in agreement to those presented in Reiter & Smith (2014). They found, using slit positions of the optical [S II] and Hα toward the HH 901,
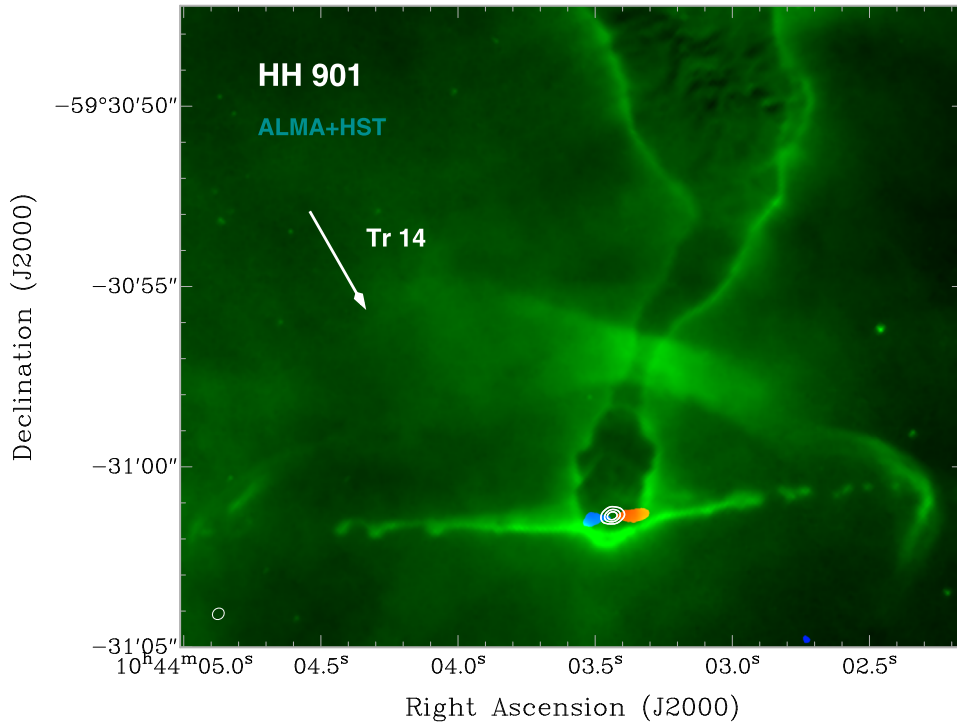
Figure 1. ALMA CO(2−1) moment zero (blue and red colors) and millimeter continuum (contours) images of the HH 901 object overlaid in a *HST*(Hα) optical image (green colors). The blue and red color represent the blueshifted and redshifted CO emission, respectively, from the HH 901 outflow. The contours range from 50% to 90% of the peak emission, in steps of 20%. The peak of the millimeter continuum emission is 2.8 mJy Beam^{-1}. Here, we are only contouring the most compact 1.3 mm emission from our observations revealing the envelope and the disk. There is still some extended emission at low levels. The half-power contour of the synthesized beam of the line image is shown in the bottom left corner. We integrate in radial velocities from +6.4 to −1.2 km s^{-1} for the redshifted emission, and from −8.2 to −14.6 km s^{-1} for the blueshifted emission for the CO outflow in the HH 901 object. The local standard rest (LSR) systemic velocity of the entire pillar associated with the object HH 901 is about −5.0 km s^{-1}.

redshifted emission in the west side of the flow with radial velocities about +25.0 km s^{-1}.

The 1.3 mm continuum image traces the disk and possibly part of the envelope at slightly larger scales. From a Gaussian fitting to the continuum source from a map obtained using a ROBUST parameter equal to 0.5 (yielding a better sensitivity), we obtained a deconvolved size of 0″.49 ± 0″.03 × 0″.33 ± 0″.03 with an PA of 100° ± 7° and an integrated flux of 6.8 ± 0.4 mJy Beam^{-1}. The corresponding physical sizes of these deconvolved values are about 700 au, which suggests that we are also seeing part of the envelope and disk. Assuming that the dust emission is optically thin and isothermal, the dust mass (M_d) is directly proportional to the flux density (S_ν) integrated over the source as

$$M_d = \frac{D^2 S_\nu}{\kappa_\nu B_\nu(T_d)}, \qquad (1)$$

where D is the distance to the Carina Nebula (2.3 ± 0.1 kpc, Smith & Brooks 2008), κ_ν the dust mass opacity, and B$_\nu(T_d)$ the Planck function for the dust temperature T$_d$. In reality, thermal dust emission is probably not optically thin, hence the estimated mass is considered to be the lower limit. Assuming a dust mass opacity (κ_ν) of 0.015 cm^2 g^{-1} (taking a dust-to-gas ratio of 100) appropriate for these wavelengths (1.3 mm; Ossenkopf & Henning 1994), a typical opacity power-law index $\beta = 1.2$ (obtained from our ALMA data), as well as a characteristic dust temperature of 50 K, we estimated a lower limit for the mass of the most compact part (i.e., not interferometrically filtered) of the disk and envelope system associated with HH 901 of about 0.1 $M_\odot$. The mass uncertainty

could be very large (a factor of up to 3 or 4) given the uncertainty in the opacity and in the dust temperature.

We can also estimate the volumetric and column density following the procedure described in Hernández-Hernández et al. (2014). We obtained a lower limit for the column density of 10^{24} cm^{-2} and a volumetric density of 10^8 cm^{-3} for the dusty source associated with the HH 901 object. These values are observed in very dense regions as compact envelopes and circumstellar disks toward the nearest giant molecular cloud (GMC), Orion (Takahashi et al. 2013; Teixeira et al. 2016).

If we assume that the continuum emission at these millimeter wavelengths is mostly arising from the disk, with a very small contribution of the envelope, the 0.1 $M_\odot$ could be linked to the disk. If we further adopt a value of M_{star}/M_{disk} between 1 and 10 (Bate 2018), we can estimate that the protostar in the middle of the HH 901 object should be a low-mass star. Furthermore, if the envelope is even more massive and the disk mass is smaller, we will have a protostar of lower mass. However, given the uncertainties on the mass estimation for the disks (a factor of 3 or 4), it could also be possible that the star in the middle is an intermediate-mass star. This is in agreement with recent observations (Reiter & Smith 2013, 2014).

In Figures 2 and 3 show the kinematics and distribution of the molecular gas using the C^{18}O, N$_2$D$^+$, and ^{12}CO spectral lines. These figures present the moment-zero emission from ^{12}CO together with the moment one of the C^{18}O, N$_2$D$^+$, and ^{12}CO lines. In order to compute these moments we integrate in radial velocities from −14.6 to +6.4 km s^{-1}, which includes the emission from the pillars and the outflows. The molecule that better traces the pillars and the outflows is ^{12}CO, see
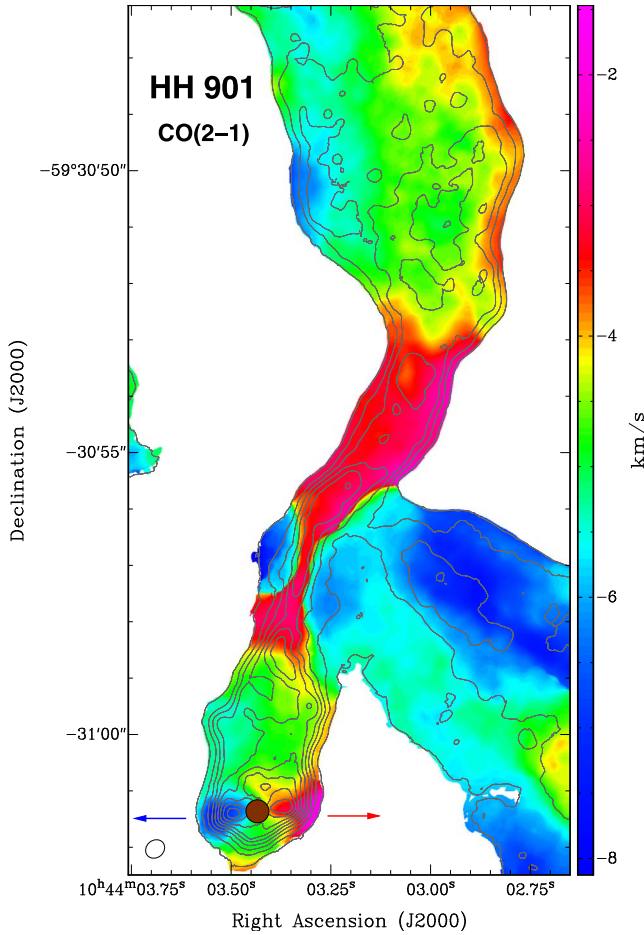
Figure 2. ALMA CO(2−1) moment zero (contours) and one (colors) maps of the pillar and outflow HH 901. The contours range from 10% to 90% of the peak emission, in steps of 10%. The peak of the millimeter line CO emission is 1.8 Jy Beam^{-1} km s^{-1}. The half-power contour of the synthesized beam of the line image is shown in the bottom left corner. The LSR radial-velocity scale bar is shown on the right. The brown circle marks the position of the disk revealed in these ALMA observations for the HH 901 object. The red and blue arrows trace the orientation of the outflow. For the CO moment-zero image, we integrate in radial velocities from −15.9 to +6.4 km s^{-1}. The LSR systemic velocity of the entire pillar associated with the object HH 901 is about −5.0 km s^{-1}.

Figure 1. From this figure, one can see how the pillar is very well defined and with a clear east–west velocity gradient going from the blueshifted to redshifted, respectively. In the southernmost side of the pillar, the bipolar outflow of HH 901 is evident. The bipolar outflow is only observed in the area traced by the pillar probably because the critical density for CO(2−1) (∼10^4 cm^{-3}) decreases drastically outside of the pillar and the outflow emission becomes too faint at larger spatial scales to be detected. Both lines, C^{18}O and N$_2$D$^+$, confirmed the east–west velocity gradient clearly revealed by the CO, as seen in Figure 3. However, for the case of N$_2$D$^+$, this molecule is only observed in a small solid angle coincident with the 1.3 mm continuum image, probably tracing the densest parts of the pillar where the star formation is taking place. The critical density of N$_2$D$^+$ $J = 3−2$ is about 3×10^6 cm^{-3}, which explains the fact that the N$_2$D$^+$ line has better spatial correlation with the 1.3 mm dust continuum emission. Matsushita et al. (2019) reported that the N$_2$D$^+$ line is strongly depleted toward the dusty massive core MM5/OMC-3 and this is explained in terms of chemical evolution. Once CO

evaporates in the gas phase, molecules like N$_2$H$^+$ or N$_2$D$^+$ will not have an efficient formation process. This is, however, not observed in our maps probably because a better angular resolution or sensitivity is needed.

As CO(2−1) is probably optically thick, we can use C^{18}O to estimate the opacity (τ_0) and then to estimate the mass of the pillar and the outflow. Assuming local thermodynamic equilibrium, we can estimate the masses using the equations presented in Scoville et al. (1986) and Palau et al. (2007) for the $J = 2−1$ transition, obtaining

$$\left[\frac{M_{H_2}}{M_\odot}\right] = 1.2 \times 10^{-15}\, T_{\text{ex}}\, e^{\frac{16.59}{T_{\text{ex}}}} X_{\frac{H_2}{CO}}$$

$$\times \left[\frac{\int I_\nu dv}{\text{Jy km s}^{-1}}\right]\left[\frac{\theta_{\text{maj}}\,\theta_{\text{min}}}{\text{arcsec}^2}\right]\left[\frac{D}{\text{pc}}\right]^2. \qquad (2)$$

We used 2.8 as mean molecular weight, an abundance ratio between the molecular hydrogen and the carbon monoxide ($X_{\frac{H_2}{CO}}$) of ∼10^4 (Scoville et al. 1986), an excitation temperature (T_{ex}) of 50 K, an average intensity (I_ν) of 0.01 Jy Beam^{-1} for the outflow, and 0.06 Jy Beam^{-1} for the pillar; we take a velocity range (dv) of 5.5 km s^{-1} for the outflow and 2.5 km s^{-1} for the pillar, and a distance (D) to the source of 2.3 ± 0.1 kpc. We then estimate a gas mass for the outflow of ∼5 × 10^{-4} $M_\odot$ and for the pillar of ∼0.1 $M_\odot$. For the mass of the outflow, we can correct this value for the inclination, therefore the true velocity range is $dv_{\text{real}} = \frac{dv}{\sin\theta}$, where θ is the inclination angle taken to be 20° (Reiter & Smith 2013, 2014), so $dv_{\text{real}} = 16$ km s^{-1} and the mass is 10^{-3} $M_\odot$.

The uncertainty in the values of the mass arises mainly from the error in the distance, which is only 4%, the flux density, which is about 10%, and the excitation temperature. Given that the C^{18}O intensity line is approximately five times weaker than the ^{12}CO line, we estimate an average opacity (τ_0) of 0.2, so we corrected the mass value by a factor of $\left[\frac{\tau_0}{1-\exp(-\tau_0)}\right]$. Furthermore, this mass estimation is in agreement with the mass obtained for the HH 901 pillar using a volumetric density of 10^5 cm^{-3} and a physical volume of 10″ × 2″ × 2″ obtained in Reiter & Smith (2013) and with a value of about 0.1 $M_\odot$.

For the outflow, the resulting kinetic energy ($E_k = \frac{1}{2}mv^2$) is about 10^{42} ergs and the momentum ($p = mv$) is 1 × 10^{-2} $M_\odot$ km s^{-1}. These values are slightly higher than those estimated by Lumbreras & Zapata (2014) and Zapata et al. (2015, 2018) for outflows associated with low-mass protostars, but possibly consistent if the correction for outflow inclination is taken into account in these studies. If we estimate the mechanical force for the outflow F$_{CO}$, we obtain a value of 1.5 × 10^{-5} $M_\odot$ yr^{-1} km s^{-1}. This value is low compared to those obtained for intermediate-mass young stars reported in Table 7 of van Kempen et al. (2016), again suggesting that this outflow is associated with a low-mass or in the limit of an intermediate star. If we add the momentum and energy from the optical counterpart it could be an intermediate-mass star. Here, it is important to mention that the outflows in Carina are strongly irradiated, and maybe most of the energy budget is already in the optical irradiated counterparts, thus a direct comparison with the outflows of van Kempen et al. (2016) could be not so straight.

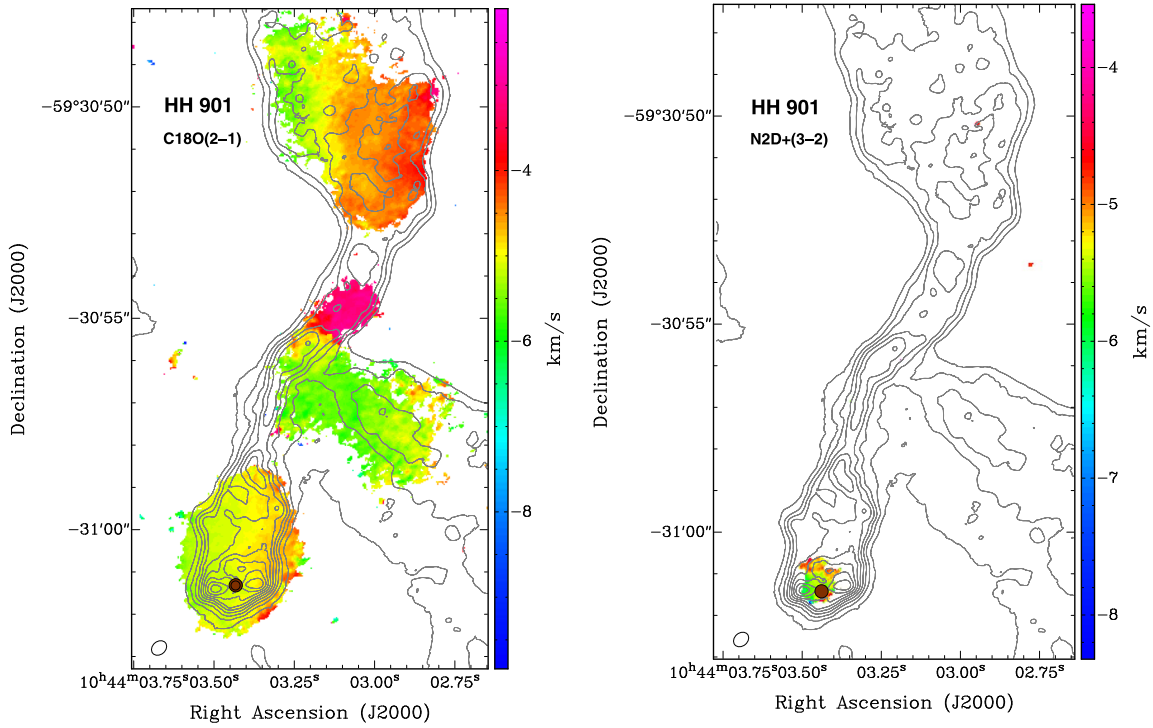As already mentioned in Section 1, Reiter & Smith (2013, 2014) suggested that the HH 901 jet is energized by a

Figure 3. ALMA $C^{18}O(2-1)$ (left panel) and $N_2D^+(3-2)$ (right panel) moment one maps overlaid with a contour image of the $CO(2-1)$ moment zero of the pillar and outflow HH 901. The contours range from 10% to 90% of the peak emission, in steps of 10%. The peak of the millimeter line CO emission is 1.8 Jy Beam^{-1} km s^{-1}. The half-power contour of the synthesized beam of the line image is shown in the bottom left corner of each panel. The LSR radial-velocity scale bar is shown on the right. The brown circle marks the position of the disk+envelope revealed in these ALMA observations for the HH 901 object.

relatively young intermediate-mass star (2–8 $M_\odot$). However, this estimation of the mass (and evolutionary stage) is very poorly constrained because they do not have direct detection of the IR flux from the driving source of HH 901 (Reiter & Smith 2014). This assumption is only inferred by the large mass-loss rates of a few 10^{-6} $M_\odot$ yr^{-1} (these are about of two orders of magnitude larger than those observed in T-Tauri stars) obtained from the optical ionized lines. These large mass-loss rates can be later transformed to mass-accretion rates and then to luminosity of the exciting star. However, the possibility that the powering source of HH 901 is of intermediate-mass is in agreement with our ALMA data, but this intermediate-mass star must be on the low range of mass as suggested by the outflow energy.

Given the high mass-loss rate reported in the HH 901 object (10^{-6} $M_\odot$ yr^{-1}), the protostar in the middle could be a Class 0/I object, so this should be very obscured even in the IR wavelengths. This is in agreement with the fact that the protostar is still surrounded by an envelope traced by the 1.3 mm and N_2D^+ emission.

Following Mesa-Delgado et al. (2016), we can estimate the photoevaphoration timescale for the pillar or globulette associated with the HH 901 object. Taken Equation (2) (already discussed in that paper), which allows us to estimate the theoretical value of the globule/disk mass photoevaporation rate $\dot{M}$ by extreme ultraviolet radiation (EUV),

$$\dot{M}_{EUV} \simeq 4 \times 10^{-9} \left(\frac{F_{EUV}}{10^{10}s^{-1}\,cm^2}\right)^{1/2}$$
$$\times \left(\frac{R}{100AU}\right)^{3/2} M_\odot yr^{-1}, \quad (3)$$

where F_{EUV} is EUV flux and R is the radius of the globule or disk. As the massive cluster Tr 14 is the closest (1.0 pc) to the HH 901 object, we ignored at this point the radiation for the massive cluster located also in this region Tr 16. The Tr 14 cluster has an UV luminosity (Q_H) of 2×10^{50} photon s^{-1} (Smith & Brooks 2008), implying $F_{EUV} = 10^{12}$ photon s^{-1} cm^{-2} at the distance of the HH 901 object. For a radius of 1000 au, and using Equation (3), we obtain a mass photoevaporation rate $\dot{M}$ equal to 1×10^{-6} $M_\odot$ yr^{-1}. Therefore, taking a mass of 0.1 $M_\odot$ for the pillar of HH 901, we obtain that the pillar will be photoevaporated in around 10^5 yr. This timescale is shorter than that estimated, for example, for the massive evaporating gas globule (EGG) or globulette 105–600 (Mesa-Delgado et al. 2016) of about 10^6 yr. However, the 105–600 globulette is further away from the Tr 14 massive cluster (17 pc), and is more massive (0.1 to 0.3 $M_\odot$), which explains the large difference.

3.2. HH 902

In Figure 4 we present the HST/ACS image from Smith et al. (2010) of the optical jet HH 902 overlaid with the ALMA high-velocity $CO(2-1)$ and the 1.3 mm continuum emission. As in the HH 901 object (Figure 1), the CO emission also reveals a bipolar and collimated outflow that is tracing the most inner part of the optical jet in a northwest and southeast orientation. This map reveals that the blueshifted emission is located toward an eastern orientation, while redshifted emission is to its western side, similar to the HH 901 object. We integrate in radial velocities from +3.7 to −5.6 km s^{-1} for the redshifted emission, and from −10.8 to −15.2 km s^{-1} for the blueshifted emission for the CO outflow in the HH 902 object.
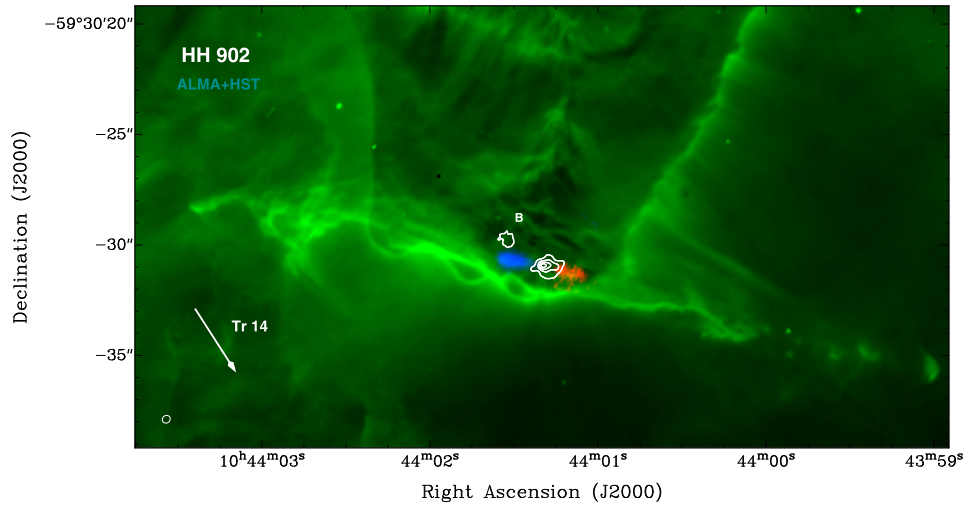
Figure 4. ALMA CO(2−1) moment zero (blue and red colors) and millimeter continuum (contours) images of the HH 902 object overlaid in an *HST* optical image (green colors). The blue and red color represent the blueshifted and redshifted emission, respectively, from the HH 902 outflow. The contours range from 50% to 80% of the peak emission, in steps of 10%. The peak of the millimeter continuum emission is 5.1 mJy Beam^{-1}. Here, we are only contouring the most compact 1.3 mm emission from our observations revealing the envelope and the disk. There is still some extended emission at low levels. The half-power contour of the synthesized beam of the continuum image is shown in the bottom left corner. We integrate in radial velocities from −3.7 to −5.6 km s^{-1} for the redshifted emission, and from −10.8 to −15.2 km s^{-1} for the blueshifted emission for the CO outflow. The LSR systemic velocity of the entire pillar associated with the object HH 902 is about −8.5 km s^{-1}.
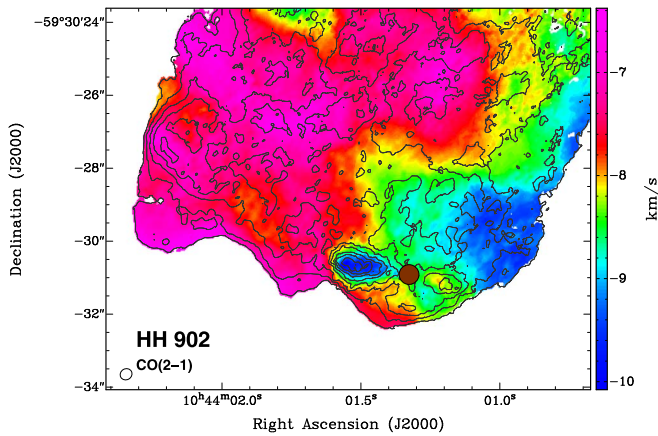

Figure 5. ALMA CO(2−1) moment zero (contours) and one (colors) maps of the pillar and outflow HH 902. The contours range from 10% to 90% of the peak emission, in steps of 10%. The peak of the millimeter line CO emission is 1.6 Jy Beam^{-1} km s^{-1}. The half-power contour of the synthesized beam of the line image is shown in the bottom left corner. The LSR radial-velocity scale bar is shown on the right. The brown circle marks the position of the disk revealed in these ALMA observations for the HH 902 object. For the CO moment-zero image, we integrate in radial velocities from −15.2 to +3.7 km s^{-1}. The LSR systemic velocity of the entire pillar associated with the object HH 902 is about −8.5 km s^{-1}.

The CO emission between −5.5 km s^{-1} and −10.7 km s^{-1} is associated with the dusty pillar as is shown in Figure 2. The LSR systemic velocity of the entire pillar associated with the object HH 902 is about −8.5 km s^{-1}. The radial velocities of the innermost CO outflow are in agreement to those presented in Reiter & Smith (2014).

The 1.3 mm continuum emission in Figure 4 is also tracing, as in Figure 1, the disk+envelope associated with the HH 902 object. However, in this figure two objects, named A and B, are revealed. Component A is associated with the HH 902 object, while component B is to its northwest. Component B is not associated with any molecular outflow, maybe because it is still

in its pre-stellar phase. This source is extended with a size of about 2000 au and has a flux density of 38 ± 2.0 mJy Beam^{-1}. Assuming a dust temperature of 30 K, this flux density corresponds to a mass of 1.5 M$_\odot$, which is likely associated with an extended envelope. For the millimeter component A, from a Gaussian fitting to the continuum source from a map obtained using ROBUST equals to 0.5 (with a better angular resolution), we obtained a deconvolved size of 0″34 ± 0″02 × 0″28 ± 0″02 with an PA of 107° ± 13° and an integrated flux of 6.5 ± 0.7 mJy Beam^{-1}. The corresponding physical sizes of these deconvolved values are about 700 au, which again suggests that we are also seeing part of the envelope and disk.

Following Equation (1) and taking similar values to the ones assumed for the object HH 901, we estimated a lower limit (because again the thermal dust emission is probably not optically thin) for the mass of the most compact part of the disk and envelope system (of component A) associated with HH 902 of about 0.1 M$_\odot$. In a similar way as for the HH 901 continuum object, this mass for the dust for the HH 902 object corresponds to a low-mass protostar.

In Figures 5 and 6, the kinematics and distribution of the molecular gas using the C^{18}O, N$_2$D$^+$, and ^{12}CO spectral lines are presented. These figures present the moment-zero emission from ^{12}CO together with the moment one of the C^{18}O, N$_2$D$^+$, and ^{12}CO lines. Similar to Figures 3 and 4, in order to compute these moments we integrate in radial velocities from −15.2 to +3.7 km s^{-1}, which includes the emission from the pillars and the outflow. The molecule that better traces the pillars and the outflow is again ^{12}CO, as seen in Figure 5, but now for the HH 902 object. From this figure, one can see how the pillar is very well defined and with a clear east–west velocity gradient going from the blueshifted to redshifted, respectively. In the most southern side of the pillar, the bipolar outflow of HH 902 is evident. Both lines, C^{18}O and N$_2$D$^+$, confirm the east–west velocity gradient clearly revealed by CO, as seen in Figure 5. However, for the case of N$_2$D$^+$, this molecule again is only observed in a small solid angle coincident with the 1.3 mm
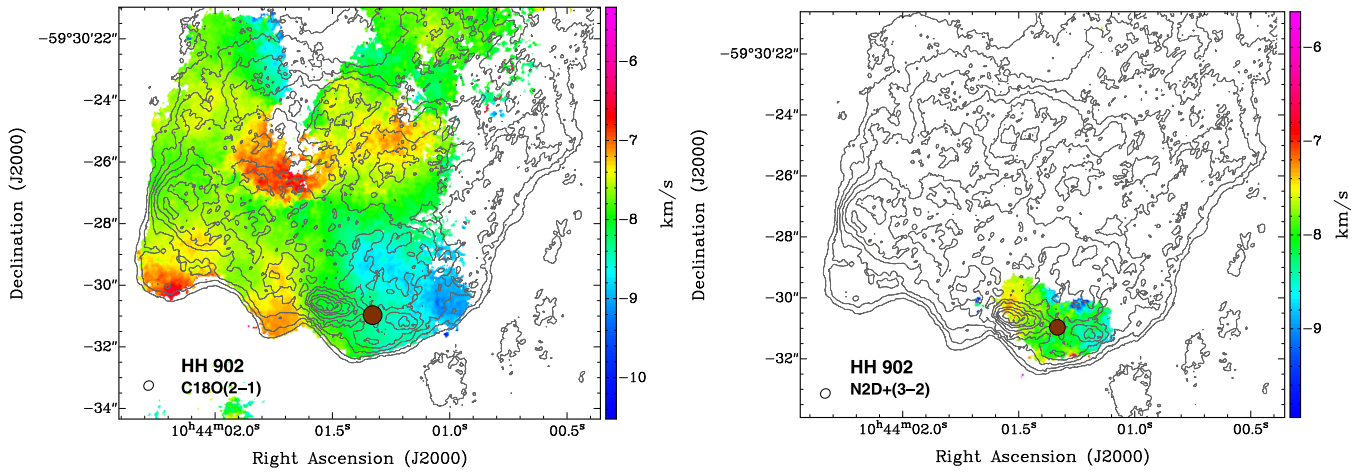
Figure 6. ALMA $C^{18}O(2-1)$ (left panel) and $N_2D^+(3-2)$ (right panel) moment one maps overlaid with a contour image of the $CO(2-1)$ moment zero of the pillar and outflow HH 902. The contours range from 10% to 90% of the peak emission, in steps of 10%. The peak of the millimeter line CO emission is 1.8 Jy Beam^{-1} km s^{-1}. The half-power contour of the synthesized beam of the line image is shown in the bottom left corner of each panel. The LSR radial-velocity scale bar is shown on the right. The brown circle marks the position of the disk+envelope revealed in these ALMA observations for the HH 902 object.

continuum image, probably tracing the densest parts of the pillar, as in the HH 901 object.

Using Equation (2) and assuming similar values for the excitation temperature, an abundance ratio, and distance, we can obtain the mass for the outflow and the pillar associated with the HH 902 object. We take an average intensity (I_ν) of 0.015 Jy Beam^{-1} for the outflow and 0.07 Jy Beam^{-1} for the pillar, and we also take a velocity range (dv) of 5.0 km s^{-1} for the outflow and 3.0 km s^{-1} for the pillar. For these values, we estimate a gas mass for the outflow of $7 \times 10^{-4} M_\odot$ and for the pillar of $\sim 0.2 M_\odot$. We also corrected these mass values by the opacity. Moreover, correcting these values by the inclination, we obtain a mass for the outflow of $10^{-3} M_\odot$.

Taking again Equation (3) and similar values for the EUV radiation ($F_{EUV} = 10^{12}$ photon s^{-1} cm^{-2}) at the distance of the HH 902 object and a radius of 4×10^3 au, we obtain a mass photoevaporation rate $\dot{M}$ equal to $1 \times 10^{-5} M_\odot$ yr^{-1}. Therefore, taking a mass of $0.2 M_\odot$ for the pillar HH 902, we obtain that the pillar will be photoevaporated in around 2×10^4 yr, which is a lower value than the timescale of the HH 901.

Given the short photoevaporated timescales of the molecular pillars and that the protostars in these pillars are still very embebed, we suggest that the disks inside of the pillars will be quickly affected by the radiation of the massive stars (in about 10^4—10^5 yr), forming proplyds like those observed in Orion (O'Dell et al. 1993, 2008; Henney and O'Dell 1999).

4. Conclusions

In this study, we present sensitive and high angular resolution observations of the famous HH 901 and HH 902 objects located in the Carina Nebula using ALMA. The main results of our work can be summarized as follows.

1. Our observations reveal for the first time, the bipolar CO collimated outflows and the dusty disks (plus envelopes) that are energizing the extended and irradiated HH 901/902 objects far from the pillars.
2. We find that the masses of the disks+envelopes are about $0.1 M_\odot$ and that of the bipolar outflows are between 10^{-3} and $10^{-4} M_\odot$, which suggest that the outflows could be energized by low- or maybe intermediate-mass protostars.

3. We also reveal the kinematics of the gas in the pillars together with their respective gas masses (0.1–$0.2 M_\odot$).
4. We estimate that the pillars will be photoevaporated in around 10^4–10^5 yr by the massive and luminous stars located in the Tr 14 cluster.

Facilities: HST(STIS), ALMA.

Software: CASA(McMullin et al. 2007), KARMA (Gooch 1996).

ORCID iDs

Luis A. Zapata ⓘ https://orcid.org/0000-0003-2343-7937
Jesús A. Toalá ⓘ https://orcid.org/0000-0002-5406-0813
Satoko Takahashi ⓘ https://orcid.org/0000-0002-7287-4343
Adal Mesa-Delgado ⓘ https://orcid.org/0000-0003-3776-6977

References

Bally, J. 2016, ARA&A, 54, 491
Bate, M. R. 2018, MNRAS, 475, 5618
Feigelson, E. D., Getman, K. V., Townsley, L. K., et al. 2011, ApJS, 194, 9
Gooch, R. 1996, in ASP Conf. Ser. 101, Astronomical Data Analysis Software and Systems V, ed. G. H. Jacoby & J. Barnes (San Fransisco, CA: ASP), 80
Haikala, L. K., Gahm, G. F., Grenman, T., et al. 2017, A&A, 602, A61
Hartigan, P., Palmer, J., & Cleeves, L. I. 2012, HEDP, 8, 313
Hartigan, P., Reiter, M., Smith, N., et al. 2015, AJ, 149, 101
Henney, W. J., & O'Dell, C. R. 1999, AJ, 118, 2350
Hernández-Hernández, V., Zapata, L., Kurtz, S., & Garay, G. 2014, ApJ, 786, 38
Lumbreras, A. M., & Zapata, L. A. 2014, AJ, 147, 72

Massey, P., & Johnson, J. 1993, AJ, 105, 980
Matsushita, Y., Takahashi, S., Machida, M. N., et al. 2019, ApJ, 871, 221
McMullin, J. P., Waters, B., Schiebel, D., Young, W., & Golap, K. 2007, in
    ASP Conf. Ser. 376, Astronomical Data Analysis Software and Systems
    XVI, ed. R. A. Shaw, F. Hill, & D. J. Bell (San Fransisco, CA: ASO), 127
Mesa-Delgado, A., Zapata, L., Henney, W. J., Puzia, T. H., & Tsamis, Y. G.
    2016, ApJL, 825, L16
O'Dell, C. R., Muench, A., Smith, N., & Zapata, L. 2008, in Handbook of Star-
    forming Regions, Vol. I, ed. B. Reipurth (San Fransisco, CA: ASP), 544
O'Dell, C. R., Wen, Z., & Hu, X. 1993, ApJ, 410, 696
Ossenkopf, V., & Henning, T. 1994, A&A, 291, 943
Palau, A., Estalella, R., Ho, P. T. P., Beuther, H., & Beltrán, M. T. 2007, A&A,
    474, 911
Povich, M. S., Smith, N., Majewski, S. R., et al. 2011, ApJS, 194, 14
Preibisch, T., Hodgkin, S., Irwin, M., et al. 2011, ApJS, 194, 10
Reiter, M., & Smith, N. 2013, MNRAS, 433, 2226
Reiter, M., & Smith, N. 2014, MNRAS, 445, 3939
Sahai, R., Güsten, R., & Morris, M. R. 2012, ApJL, 761, L21
Scoville, N. Z., Sargent, A. I., Sanders, D. B., et al. 1986, ApJ, 303, 416
Smith, N. 2006, MNRAS, 367, 763
Smith, N., Bally, J., & Walborn, N. R. 2010, MNRAS, 405, 1153
Smith, N., & Brooks, K. J. 2008, in Handbook of Star-forming Regions, Vol.
    II, ed. B. Reipurth (San Fransisco, CA: ASP), 138
Takahashi, S., Ho, P. T. P., Teixeira, P. S., et al. 2013, ApJ, 763, 57
Teixeira, P. S., Takahashi, S., Zapata, L. A., & Ho, P. T. P. 2016, A&A,
    587, A47
van Kempen, T. A., Hogerheijde, M. R., van Dishoeck, E. F., et al. 2016,
    A&A, 587, A17
Walborn, N. R. 1973, ApJ, 179, 517
Walborn, N. R. 1995, RmXAC, 2, 51
Zapata, L. A., Fernández-López, M., Rodríguez, L. F., et al. 2018, AJ, 156, 239
Zapata, L. A., Lizano, S., Rodríguez, L. F., et al. 2015, ApJ, 798, 131